

Study of Cosmogenic Neutron Production for ~ 360 GeV Muons

Xinshun Zhang,^{1,2} Jinjing Li,^{1,2,†} Shaomin Chen,^{1,2,3} Wei Dou,^{1,2} Haoyang Fu,^{1,2} Ye Liang,^{1,2} Qian Liu,⁴ Wentai Luo,^{1,2} Ming Qi,⁵ Wenhui Shao,^{1,2} Haozhe Sun,^{1,2} Jian Tang,⁶ Yuyi Wang,^{1,2} Zhe Wang,^{1,2,3} Changxu Wei,^{1,2} Jun Weng,^{1,2} Yiyang Wu,^{1,2} Benda Xu,^{1,2,3} Chuang Xu,^{1,2} Tong Xu,^{1,2} Yuzi Yang,^{1,2} Aiqiang Zhang,^{1,2} and Bin Zhang^{1,2}
(JNE Collaboration)

¹*Department of Engineering Physics, Tsinghua University, Beijing 100084, China*

²*Center for High Energy Physics, Tsinghua University, Beijing 100084, China*

³*Key Laboratory of Particle & Radiation Imaging (Tsinghua University), Ministry of Education, China*

⁴*School of Physical Sciences, University of Chinese Academy of Sciences, Beijing 100049, China*

⁵*School of Physics, Nanjing University, Nanjing 210093, China*

⁶*School of Physics, Sun Yat-Sen University, Guangzhou 510275, China*

(Dated: September 9, 2024)

The China Jinping underground Laboratory (CJPL) is an excellent location for studying solar, terrestrial, and supernova neutrinos due to its 2400-meter vertical rock overburden. Its unparalleled depth gives an opportunity to investigate the cosmic-ray muons with exceptionally high average energy at ~ 360 GeV. This paper details a study of muon-related backgrounds based on 1178 days of data collected by the 1-ton prototype neutrino detector used for the Jinping Neutrino Experiment (JNE) since 2017. The apparent effects of detectors' finite size on the measured result are first discussed in detail. The analysis of 493 cosmic-ray muon candidates and 13.6 ± 5.7 cosmogenic neutron candidates, along with a thorough evaluation of detection efficiency and uncertainties, gives a muon flux of $(3.56 \pm 0.16_{\text{stat.}} \pm 0.10_{\text{sys.}}) \times 10^{-10} \text{ cm}^{-2} \text{ s}^{-1}$ and a cosmogenic neutron yield of $(3.37 \pm 1.41_{\text{stat.}} \pm 0.31_{\text{sys.}}) \times 10^{-4} \mu^{-1} \text{ g}^{-1} \text{ cm}^2$ in LAB-based liquid scintillator.

PACS numbers: 14.60.Pq, 29.40.Mc, 28.50.Hw, 13.15.+g

Keywords: Jinping Neutrino Experiment, liquid scintillator, cosmogenic neutron, muon flux

I. INTRODUCTION

Situated in the Jinping Mountains of Sichuan, China, with a vertical rock overburden of about 2400 meters, the China Jinping Underground Laboratory (CJPL) is one of the world's deepest underground laboratories [1]. This unparalleled depth provides exceptional shielding from cosmic rays, which is crucial for detecting solar neutrinos and various rare signals.

The Jinping Neutrino Experiment (JNE) aims to study MeV-scale neutrinos, such as solar, terrestrial, and supernova neutrinos, etc., which are highly sensitive to muons and the cosmogenic radioactive backgrounds [2]. For example, in organic scintillators, ^{11}C can be produced by cosmic muons through spallation processes on ^{12}C . A detailed discussion of the related processes can be found in Ref. [3]. The β^+ -decays of ^{11}C are largely indistinguishable from neutrino-induced electron recoils, presenting a challenge for the observation of Carbon-Oxygen-Nitrogen solar neutrinos [4, 5]. The cosmic-ray spallation products also act as an important background in searches for the upturn of the solar ^8B neutrino spectrum [6, 7] and supernova relic neutrinos [8]. Among those products, cosmogenic neutrons, created in nuclear interactions triggered by cosmic muons, are significant backgrounds for many rare-event searches, even in deep underground detector [9]. Therefore, it is important to investigate the production and properties of cosmogenic neutrons at CJPL, as the depth results in significantly elevated average muon energy. Furthermore, the muon flux can differ significantly between laboratories lo-

cated under mountains and those below mine shafts with the same vertical rock overburden [10]. A better understanding of cosmic muon flux and neutron yield is crucial for optimizing the design of future neutrino detectors' active and passive shielding at CJPL.

A 1-ton scintillator detector, built as a prototype for the JNE, has been operational since 2017 at the first construction phase of CJPL (CJPL-I). This detector is designed to evaluate the performance of key components and technologies, and measure the underground background levels in situ [11]. This study utilized this 1-ton prototype to measure the cosmic-ray muon flux and cosmogenic neutron yield in linear alkylbenzene (LAB)-based liquid scintillator at CJPL-I, providing a comprehensive understanding of cosmic-ray muon and cosmogenic neutrons with the mountain's topography around the laboratory. Furthermore, this study gives a detailed study of the effect induced by detector's finite-size in the measurement of cosmogenic production yield firstly.

Following the detailed description of the design and operational aspects of the 1-ton prototype provided in Section II, Section III presents the simulations undertaken to model the passage of muons through the Jinping mountain and their interactions within the detector. In Section IV, we outline the preliminary data analysis procedures, including data quality assessments and the methodologies employed for event reconstruction. Section V delves into the muon candidate selection and reconstruction. The analysis details and measurement result of cosmogenic neutron yield are discussed in Section VI. Finally, Section VII provides a summary of the findings and discusses prospects.

[†] Corresponding author: jinjing-li@mail.tsinghua.edu.cn

II. THE 1-TON PROTOTYPE

Fig. 1 depicts the structural design of the 1-ton prototype [12]. The central target volume is encompassed by a 645-mm-radius spherical acrylic vessel with a thickness of 20 mm. This vessel contains the slow liquid scintillator (LS), which is composed of LAB as a solvent, doped with 0.07 g/L of the fluor 2,5-diphenyloxazole (PPO) and 13 mg/L of the wavelength shifter 1,4-bis(2-methylstyryl)benzene (bis-MSB). This scintillator can emit scintillation light with an extended duration, which helps in separating Cherenkov light from scintillation light [13, 14].

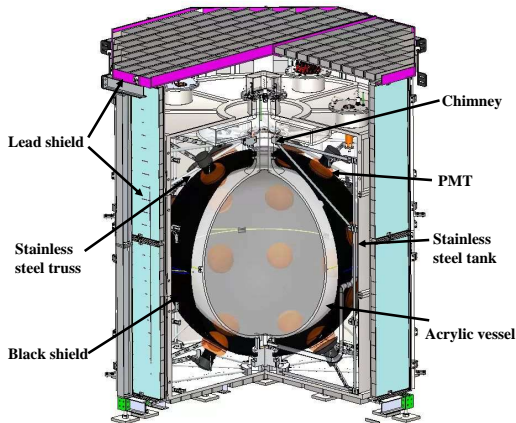


FIG. 1. The schematic figure of the 1-ton prototype for JNE.

The target volume is encompassed by pure water held within a stainless steel tank that is 4 mm thick, and has a diameter of 2000 mm, and a height of 2090 mm. Within the water, there are thirty 8-inch Hamamatsu R5912 photomultiplier tubes (PMTs) oriented inward to detect the photons emitted from the target. The water serves as an active muon veto and a passive shield against external radiation. The tank is further enclosed by a 5-cm-thick lead wall, offering additional shielding to suppress ambient radioactive background.

After two-year data collection period, we observed the β - α cascade decay of ^{214}Bi - ^{214}Po near the chimney at the top indicating the external radon gas leakage into the target volume. To shield against this background, we installed a nitrogen bubbling system to maintain positive pressure inside the detector, thus preventing air infiltration into the acrylic vessel. This system offers us an additional benefit - an increase of light yield in the LS, as the degassing process with nitrogen effectively removed dissolved oxygen from the target volume, thereby reducing the quenching effect.

The front-end electronic system consisted of four CAEN V1751 FlashADC boards and a CAEN V1495 logical trigger module. Each FlashADC board had eight channels, 10-bit ADC precision for a 1 V dynamic range, and a 1 GHz sampling rate. All PMT signals were directly fed into the FlashADC boards for digitization. If more than N_{PMT} PMTs were triggered with a voltage threshold of H_{th} -mV, the data acquisition (DAQ) system recorded the pulse shapes of all the

activated PMTs within a T_w -ns time window. The specific values are listed in Table I. Further details about the detector system can be found in Ref. [11].

III. SIMULATION

To evaluate the detection efficiencies of cosmic-ray muons and cosmogenic neutrons, we need to understand their responses in the detector. We have developed a GEANT4-based Monte Carlo (MC) simulation framework to analyze the muon interaction processes within the surrounding mountain rock and the detector materials [15, 16]. The simulations are divided into two main parts: mountain-related simulation and detector-related simulation. The first one gives the cosmic-ray muons' energy and angular distributions as they arrive the underground laboratory, with the surrounding mountain terrain incorporated. The second one uses a muon generator informed by the mountain simulation results, producing processed PMT waveforms from the electronics for each event, with features close to the real data.

A. Mountain Related Simulation

The mountain simulation uses two primary muon generators: the Modified Gaisser's formula, which works well at low energies [17], and MCEq, which numerically calculates the propagation and interactions of cosmic rays in the atmosphere [18, 19]. Given the overburden depth of CJPL, approximately 2400 m, muons reaching the laboratory require relatively high initial kinetic energy (on the order of TeV), where the Modified Gaisser's formula is not sufficiently accurate. Therefore, we use the results from the MCEq simulation as the nominal ones.

The terrain data of the Jinping mountain region is sourced from the NASA SRTM3 dataset [20]. The mountain terrain is accurately integrated into the GEANT4 geometry using the Delaunay Triangulation method. This method can group discrete elevation points into triangles to model the mountain surface. Two figures in Fig. 2 show the contour map and the 3D representation of the mountain structure near CJPL-I. In simulation, the mountain is assumed to consist of a uniform density of rock set to 2.8 g/cm^3 [21]. The rock composition is 46.1% oxygen, 28.2% silicon, 8.2% aluminum, and 5.6% iron, aligning with the typical abundance found in Earth's crust [22]. Fig. 3 shows the simulated energy and angular distributions of muons arriving CJPL-I.

B. Detector Related Simulation

The detector-related simulation, including the LS, the PMTs, and the electronics, utilizes the mountain-related simulation results as input. The waveform saturation effect due to the significant particle energy deposits is also simulated. The same analysis procedures used in data, are applied to the simulation data to estimate efficiencies.

TABLE I. The details of each DAQ phase for the 1-ton prototype. T_{DAQ} : effective DAQ time. N_{PMT} : least number of the fired PMTs for trigger. T_w : sampling length of the waveform in a single channel. H_{th} : trigger threshold of a single channel. Nitrogen bubbling: presence of nitrogen bubbling system.

Start Date	End Date	T_{DAQ} [day]	N_{PMT}	T_w [ns]	H_{th} [mV]	Nitrogen Bubbling
2017-07-31	2018-10-14	392.0	25	1029	10	No
2018-10-15	2019-06-29	238.5	25	1029	5	No
2019-06-30	2019-07-14	12.6	10	600	5	No
2019-07-15	2023-09-02	534.9	10	600	5	Yes

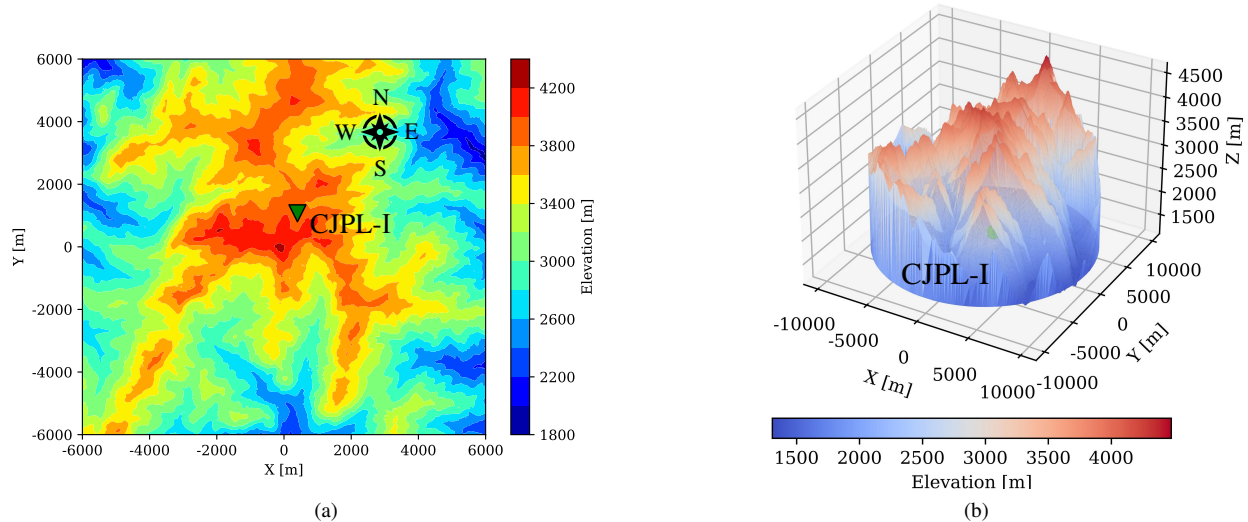


FIG. 2. (a): Contour map of mountain terrain near CJPL, given by the SRTM3 dataset [20]. (b): The mountain geometry obtained from the Delaunay Triangulation of mountain terrain in the mountain simulation. The positive direction on the x-axis corresponds to true East, and the positive direction on the y-axis corresponds to true North. The z-axis is the absolute elevation. The green point represents the position of CJPL-I.

Fig. 4 shows schematic diagram of the geometry setup for the detector simulation. Outside the detector, we add a 1-meter-thick layer of rock to account for the muon shower, which can affect the measurement of cosmic-ray muon flux and cosmogenic neutron yield.

All tracks of secondary particles involved in neutron production are recorded to correct the number of measured cosmogenic neutrons in the LS. Neutrons generated by muons in hadron showers are dominant [23]. Three physics lists are employed to address this process: QGSP-BIC-HP, QGSP-BERT-HP, and FTFP-BERT-HP. The Quark-Gluon String model (QGS) and the FRITIOF String model (FTF) are used for hadronic interactions at high energies (> 10 GeV), while the Binary Cascade model (BIC) and the Bertini Cascade model (BERT) are applied for hadronic interactions at lower energies (between 70 MeV and 9.9 GeV). The physical processes below 70 MeV and nuclear de-excitation are simulated using GEANT4's precompound model. A high-precision neutron model (HP) is used for neutron elastic and inelastic interactions below 20 MeV. The uncertainties using different physics lists are evaluated by comparing these models and will be discussed in Sec. VI.

The simulation results will be compared to the measurements in the following sections.

IV. DATA ANALYSIS

A. Data Sets

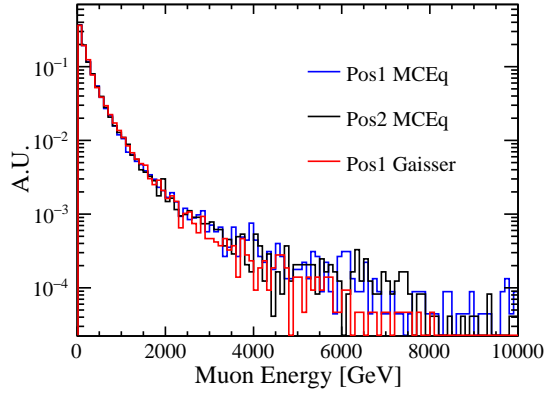
This study uses the complete dataset collected by the detector from July 31, 2017, to September 2, 2023. The detector was then decommissioned and disassembled for further upgrade. Table I summarizes the detailed run operations and conditions.

B. Data Quality

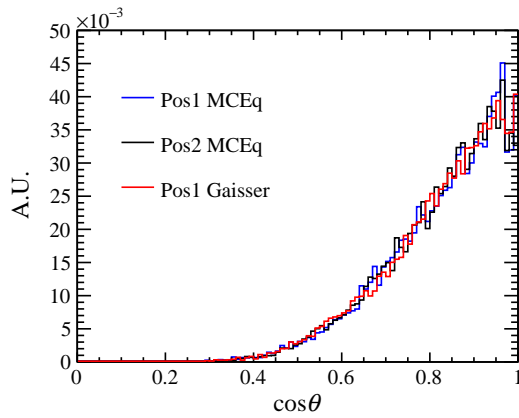
Data quality is ensured through a two-step checking process, with the minimal unit being a ~ 200 MB file typically spanning about 5 minutes under the current trigger conditions. However, the exact duration depends on the actual event rate.

The first step involves physics run selection. The analysis manually excludes the runs affected by pedestal calibration, detector maintenance, hardware issues, or external disturbances.

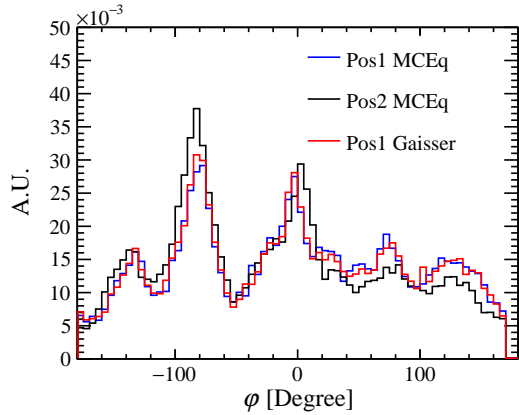
The second step is identifying bad channels based on baseline fluctuation and channel occupancy. The size of baseline fluctuation is measured by the standard deviation of base-



(a)



(b)



(c)

FIG. 3. The energy and angular distributions of muons arriving at the underground laboratory derived from the simulation. θ represents the zenith angle, defined as the angular distance from the vertical, while φ denotes the azimuthal angle, defined as the angular distance from true North in the horizontal plane. Pos1 corresponds to the location of CJPL-I, and Pos2 is situated 100 meters south of CJPL-I. Two muon models, MCEq and the Modified Gaisser Formula are used.

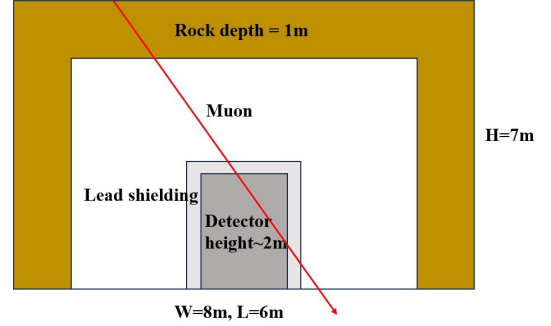


FIG. 4. The geometry setup in the detector simulation.

line, and any channel with a fluctuation exceeding 2.5 mV is marked as a bad channel. Given that the mean baseline fluctuation for a normal channel is less than 1 mV, the 2.5-mV threshold effectively identifies channels affected by electronic noise or detector malfunctions. Channel occupancy is defined as the ratio for the number of channel triggers divided by the total number of trigger events over a unit file. Given the spherical symmetry of the detector and the uniform distribution of the PMTs' positions, the occupancies are expected to be uniform. Any channel whose occupancy deviates from the average occupancy by more than 5σ is marked as a bad channel. If more than 4 bad channels are found within a unit file, that file will be removed in the following analysis.

These checks exclude about 4.9% of the data, resulting in an effective DAQ time of ~ 1178.0 days for subsequent analysis. Reductions in effective DAQ time fraction can result from a good run list or the runs with more than 4 bad channels. Events in unit files with no more than 4 bad channels are included in the study but require reconstruction with bad channel correction.

C. PMT Calibrations

The gain and time calibrations of PMT rely on the dark noise of the PMTs and the natural decay products of radioisotopes within the detector, as detailed in Ref. [11].

A real-time gain calibration is performed using the "RollingGain" method. This method calculates the charge distribution of dark noise within a given period. It is fitted using a probability distribution function that accounts for the signal generated by thermionic emission electrons from the photocathode and potential background noise [24]. The gain factor for each channel during this period is derived from the fitting result and is used to convert the measured charge into the number of photoelectrons (PE). By accumulating PEs from the good channels, the deposited energy is reconstructed in terms of the PE numbers.

The time delay between the PMT hits and the readout varies channel by channel. Therefore, time calibration is crucial

when determining the sequence of PMT hit times for event reconstruction. The sample for the calibration is selected by requiring a relatively large PE number and vertex close to the detector center. The time calibration finally provides the relative offsets among different channels. The typical value is within ± 5 ns.

D. Energy Scale

We utilize the 2.61-MeV γ peak from ^{208}Tl decay inside detector to perform the energy scale calibration. The fitted peak position gives the corresponding PE number, which can be used to determine the nominal energy scale calibration factor. This factor was determined to be 61.07 PE/MeV before July 14, 2019, and then increased to 88.02 PE/MeV due to the nitrogen bubbling between July 15, 2019, and July 22, 2019. Finally, it became stable at 99.89 PE/MeV. To cross-validate these values, we further fit the spectrum of α particles from ^{214}Po decay, and the 1.46-MeV γ rays from ^{40}K decay to evaluate the calibration factor independently. The differences between the nominal energy scale factors and those derived from the two independent samples are within 5% throughout the dataset, which is assigned as the systematic uncertainty.

V. COSMIC RAY MUON

A. Event Selection

In this analysis, all the muon candidates are required to have a visible energy exceeding 60 MeV. At this energy level, the primary backgrounds include spontaneous light emission from PMTs (flashers) and electronic noise, which can be excluded by further analysis of the charge pattern and waveform structure.

When a flasher occurs, neighboring PMTs are also likely to be illuminated. Its charge distribution is less uniform across channels than muon events, with the discharge channel collecting a significantly higher charge than others. We define a parameter $r_{\text{max}} \equiv P_{\text{max}} / \sum_{i=1}^{30} P_i$ to identify this background, where P_{max} is the maximal PE number, and P_i is the PE number of channel i , calibrated by the gain factor.

Electronic noises caused by accidental external disturbances to the detector's electronic system can lead to extreme baseline fluctuations across all channels. These fluctuations can generate triggers, mimicking high-energy signals. The mean peak number n_{peak} of the waveforms from the effective channels in an event is used to identify electronic noises. For normal events, the peak number is related to the arrival photons registered by the PMTs and is approximately proportional to the deposited energy. However, the peak number for electronic noise is significantly higher than a normal event can have. Electronic noises caused by accidental external disturbances to the detector's electronic system can lead to extreme baseline fluctuations across all channels. These fluctuations can generate triggers, mimicking high-energy signals. The

mean peak number n_{peak} of the waveforms from the effective channels in an event is used to identify electronic noises. For normal events, the peak number is related to the arrival photons registered by the PMTs and is approximately proportional to the deposited energy. However, the peak number for electronic noise is significantly higher than a normal event can have.

The distribution of r_{max} versus n_{peak} is shown in Fig. 5. By comparing simulated muon events with the data, we require $r_{\text{max}} < 0.15$ to suppress flashers and $n_{\text{peak}} < 40$ to reject electronic noise. These selection criteria are validated using MC sample.

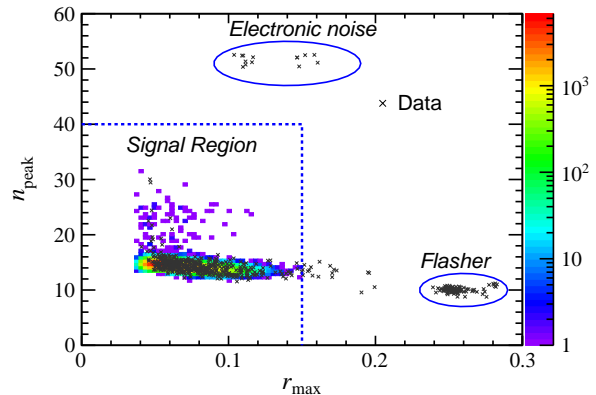


FIG. 5. r_{max} versus n_{peak} in the data (black cross) and simulation (color block). The color bar represents the number of counts in the simulation. Typical muon candidates are in the region for $r_{\text{max}} < 0.15$ and $n_{\text{peak}} < 40$, while flasher and electronic noise events have larger r_{max} and n_{peak} , which are distributed in the blue circled region.

This analysis selects 493 muon candidates, corresponding to an observed event rate of 0.42 events per day. Fig. 6 shows distribution of measured visible energy for muons in data and MC sample. Due to the waveform saturation and the energy non-linearity effect, the reconstructed energy of muons in the detector is less than the deposited one, which is especially significant for high-energy events. The average energy of muons detected in this study was investigated using GEANT4 simulations, yielding approximately 340 GeV before and 360 GeV after applying the selection criteria. The latter value, which differs from the former one reported in the previous study [25], is used in this work.

B. Direction Reconstruction

This study uses a template-based method to reconstruct the muon direction [26]. The templates are generated using the detector simulation with a uniform muon direction, each tagged with the muon direction and the entry point on the acrylic vessel. The muon direction and entry point on the vessel surface are sampled uniformly from a hemisphere facing the muon direction. The PMT arrival time pattern vector is

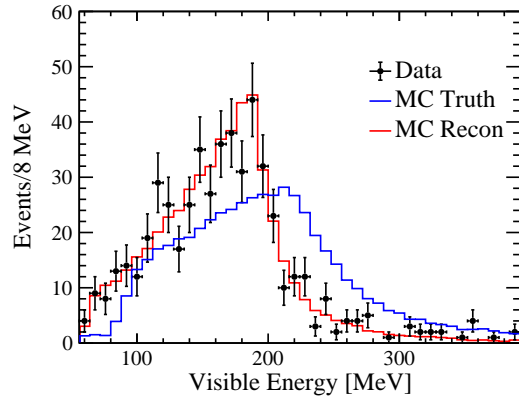


FIG. 6. The visible energy distribution of selected muon events in data (block dots) and simulation. The blue line represents the true deposited energy of muons in MC sample while the red line shows the reconstructed energy of muons in MC sample.

constructed for each template and zero-centered by subtracting the mean value. This process allowed for the comparison between the template data and the actual data using Euclidean distance to identify the 1-nearest neighbors. The muon direction is then reconstructed by calculating the weighted average of these nearest neighbors. The reconstructed distributions of the azimuth and zenith angles for both data and simulation are consistent, as shown in Fig. 7, revealing variations due to the mountain structure above CJPL-I. The detailed difference between data and simulation may result from the cavities inside the mountain like the tunnels [27].

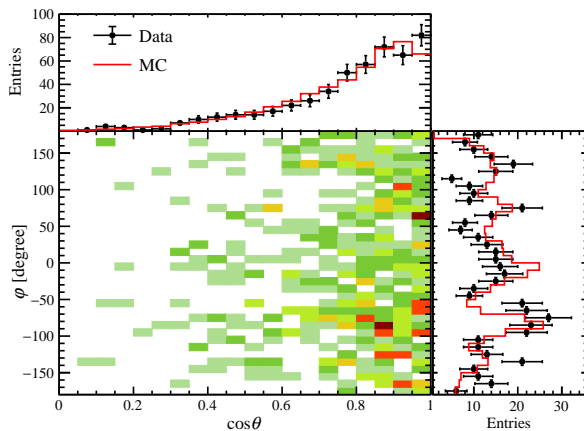


FIG. 7. The reconstructed muons' angular distribution in the data (black dots) and simulation (red line). θ and φ correspond to the zenith and azimuth angle, respectively. The one-dimensional projections are also plotted.

C. Detection Efficiency

The overall efficiency, ε , is the ratio of muons passing the selection criteria described above to the total number of muons arriving the experiment hall. Besides the muons passing directly through the detector, those interacting with the surrounding rock and lead shielding can produce showers with secondary high-energy particles, affecting the efficiency. Therefore, the entire experiment hall is considered in the simulation to account for this effect. We decompose the efficiency ε into three components: the geometry efficiency ε_g , the detection efficiency ε_d , and the shower efficiency ε_s , as

$$\varepsilon = \varepsilon_g \times \varepsilon_d + \varepsilon_s, \quad (1)$$

$$\varepsilon_g = \frac{N_p}{N_{\text{total}}}, \varepsilon_d = \frac{N_d}{N_p}, \varepsilon_s = \frac{N_s}{N_{\text{total}}}, \quad (2)$$

where N_{total} is the total number of generated muons, N_p is the number of muons passing through the sensitive volume of the detector, N_d is the number of detected muons passing the selection criteria, N_s is the number of detected muon showers passing the selection criteria.

According to the detector simulation mentioned above, the efficiencies are calculated to be $\varepsilon = 1.7\%$, $\varepsilon_g = 2.1\%$, $\varepsilon_d = 82.2\%$ and $\varepsilon_s = 0.3\%$, respectively.

D. Result and Uncertainties of Muon Flux Measurement

The cosmic muon flux at CJPL-I can be calculated as

$$\phi_\mu = \frac{N_{\text{total}}}{T \times S} = \frac{N_\mu}{\varepsilon \times S \times T}, \quad (3)$$

where N_μ is the number of selected candidates in data, T is the effective DAQ time, S is the projection area of experiment hall and is calculated to be 78.7 m^2 at CJPL-I using the angular distribution of underground muons [26].

The uncertainties are summarized in Table II. The dominant systematic uncertainty is from the variations in the energy scale, acrylic vessel radius, and CJPL-I's latitude and longitude.

TABLE II. Systematic uncertainty of flux measurement

Source	Uncertainty	Flux Uncertainty
Energy scale	$\pm 5\%$	$\pm 1.6\%$
Acrylic vessel radius	$\pm 0.5 \text{ cm}$	$\pm 1.5\%$
Lead shielding thickness	$\pm 5 \text{ cm}$	$\pm 0.2\%$
Rock thickness	$\pm 50 \text{ cm}$	$\pm 0.7\%$
Hadronic model	$\pm 50\%$	$\pm 0.5\%$
Muon generator		$\pm 0.2\%$
Latitude and longitude	$\pm 100 \text{ m}$	$\pm 1.1\%$
Elevation	$\pm 100 \text{ m}$	$\pm 0.6\%$
Total		$\pm 2.7\%$

The energy scale uncertainty is determined to be 5% at the low energy region ($\sim 1 \text{ MeV}$). However, the energy scale factor in the unit of PE/MeV is lower for the muon events, due

to the waveform saturation and energy non-linearity effect. Therefore, the energy scale for muons in simulation is fine-tuned by a binned χ^2 minimization method to make the energy distribution consistent with data. The χ^2 is defined as,

$$\chi^2 = \sum_i \frac{[n_{\text{data}}^i - n_{\text{sim}}^i(\eta)]^2}{n_{\text{data}}^i}, \quad (4)$$

where n_{data}^i is the number of events in the i -th bin of the energy distribution of data, $n_{\text{sim}}^i(\eta)$ is the number of events in the i -th bin of the energy distribution of the MC sample, η is the additional energy scale shift applied in an event-by-event basis for the MC sample. The uncertainty on η is determined to be its variation between χ_{min}^2 and $\chi_{\text{min}}^2 + 1$. The fitting provides that $\eta = 0.87 \pm 0.01$, presenting the effects from the energy non-linearity and waveform saturation. Given that this uncertainty, i.e., $\sim 1\%$ is apparently smaller than the energy scale uncertainty, the final analysis still adopts the 5% uncertainty for the energy scale. The corresponding muon flux uncertainty is estimated to be 1.6%.

The radius of acrylic vessel constrains the target volume directly affects the deposited energy of muons. In the production of the acrylic vessel, the machining accuracy of radius is about 0.5 cm, which is set as the uncertainty of this parameter. In simulation geometry, a 0.5 cm variation is set for both inner and outer radius simultaneously, resulting in a 1.5% uncertainty for muon flux.

The thickness of lead shielding and rock can affect the contribution of muon showers. The lead shielding is arranged brick by brick. There should be a tiny difference between the actual detector geometry and that used in GEANT4 simulation, where the lead shielding is considered as a perfect circular cylindrical shell. Assuming a 5 cm thickness variation conservatively, which is the typical size of a lead brick, it contributes little uncertainty to the overall efficiency.

The rock thickness of the laboratory in the simulation is set to be 1 m and varied by ± 0.5 m thickness to validate this arrangement. The variation is found to have little impact on the overall efficiency. The average free path of neutrons at 50 MeV is theoretically calculated to be about 10 cm in the rock around CJPL-I, indicating the rock's thickness is reasonable for the study of the muon shower effect. The uncertainty of secondary particle yield in muon showers is conservatively taken to be 50% for uncertainty from the hadronic models to describe the physical processes of muon showers generation. Only a 0.5% uncertainty to the muon flux is found.

The projection area of the experiment hall is sensitive to the angular distribution of underground muon. Therefore, the different inputs of underground muon can change the calculation result. Due to the complexity of the tunnel direction and the overburden terrain at CJPL-I, the accurate location of laboratory is hard to be obtained. We varied the location of the laboratory around the nominal one in latitude, longitude and elevation to study the effects. Additionally, the primary muon generators, modified Gaisser's formula and MCEq, are implemented separately, confirming that the induced difference in the projection area is negligible.

Using the selected muon candidates and considering the

systematic uncertainties described above, we measure the cosmic ray flux at CJPL-I to be

$$\phi_\mu = (3.56 \pm 0.16_{\text{stat.}} \pm 0.10_{\text{syst.}}) \times 10^{-10} \text{ cm}^{-2}\text{s}^{-1}. \quad (5)$$

This measurement is in excellent agreement with the previous one, but the precision is increased by $\sim 25\%$.

VI. MEASUREMENT OF COSMOGENIC NEUTRON YIELD IN LIQUID SCINTILLATOR

Cosmogenic neutrons are primarily generated in hadronic and electromagnetic showers that result from the passage of high-energy cosmic muons [23]. The neutron yield induced by muons is defined as the production rate of neutrons per unit muon track length per unit target density [9] and can be expressed as

$$Y_n = \frac{N_n}{(\sum L_\mu) \times \rho} = \frac{N_n}{N_\mu \times L_{\text{avg}} \times \rho}, \quad (6)$$

where N_n represents the number of neutrons generated directly or indirectly when muons pass through the target volume, N_μ denotes the number of muons traversing the target volume, L_{avg} is the average path length of muons within the target volume, and ρ signifies the density of the material.

In LS, the neutrons produced by muons can be captured by hydrogen ($n\text{H}$) after thermalization and emit a 2.2-MeV γ . The cascade between muon and this typical γ is used to tag the cosmogenic neutron events in the detector. Further efficiencies and corrections are needed to calculate N_n based on the number of observed neutron events, N_{obs} , including the non-target factor for neutron capture on non-target volumes $f_{\text{non-target}}$, shower factor f_{shower} , neutron spill factor f_{spill} , detector finite-size factor f_{size} , and also the neutron detection efficiency ε_{nt} and time selection efficiency ε_{t} . These correction factors and efficiencies will be elaborated in Sec. VIC. The overall relationship can be written as

$$N_n = N_{\text{obs}} \times \frac{(1 - f_{\text{non-target}}) \times (1 - f_{\text{shower}}) \times f_{\text{spill}}}{\varepsilon_{\text{nt}} \times \varepsilon_{\text{t}} \times f_{\text{size}}}. \quad (7)$$

A. Event Selection

Events following the muon signals tagged before are considered as neutron candidates. The time interval t_n between a neutron candidate and its preceding muon event must be within the range of [20, 1020] μs , and the energy of neutron candidate must be within the range of [0, 4] MeV. The lower bound of t_n excludes after-pulses, significant baseline fluctuations caused by the muon's passage, and cosmogenic nuclei with short lifetimes. The upper bound of t_n ensures the correlation between the muon and the 2.2-MeV γ emitted by $n\text{H}$ capture, typically occurring with a capture time of approximately 200 μs . In this study, the number of neutrons candidates m passing the selection criteria is 68.

B. Background Determination

The neutron candidates include lots of accidental coincidences from natural radioactivity. We used an unbinned likelihood fit method with the two-dimension distribution of energy and time interval t_n to determine N_{obs} . Assuming the number of neutron candidates follows a Poisson distribution with an expected value of ν , the likelihood function can be expressed as shown in Eq. 8, with the energy and time distributions treated as independent.

$$\mathcal{L} = \frac{\nu^m}{m!} e^{-\nu} \prod_{i=1}^m [f_1(E_i, \kappa) f_2(t_i)] N(\kappa), \quad (8)$$

where i represents the i -th selected events in the data, $f_1(E_i, \kappa)$ represents the energy distribution of neutron candidates, and $f_2(t_i)$ represents the time distribution, $N(\kappa)$ is the zero-centered Gaussian distribution with a 5% standard deviation, accounting for the uncertainty from energy scale.

The energy distribution is defined as

$$f_1(E, \kappa) = \omega f_s[E(1 + \kappa)] + (1 - \omega) f_b[E(1 + \kappa)], \quad (9)$$

where ω is the ratio of the signal rate to the total event rate, f_s is the probability density function of $n\text{H}$ capture gamma signals using a calorimeter function, which can well describe both the complete and partial absorption of gamma energy in the detector [28], f_b is the distribution of the backgrounds from accidental coincidences. The background spectrum is estimated by analyzing events far from the muon events in time. To enhance the background statistics, we set the time window for background selection to $[2000, 12000] \mu\text{s}$ after the preceding muon. Besides the peak of 2.61-MeV γ from ^{208}Tl decay, there are two more peaks in the background distribution around 0.2 MeV and 1.4 MeV originating from the two trigger thresholds in different periods of the detector.

The distribution of time interval t_n is described by

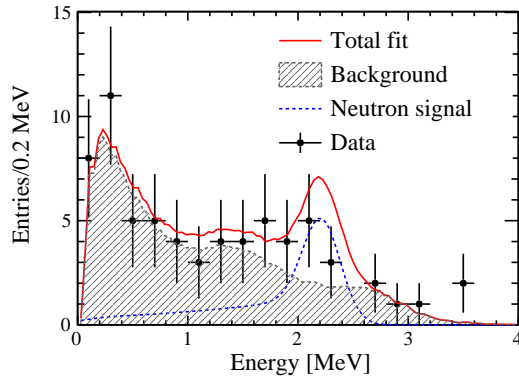
$$f_2(t) = \omega A e^{-t_n/\tau_n} + (1 - \omega) B, \quad (10)$$

where τ_n is the mean $n\text{H}$ capture time, A and B are the normalization factors for exponential and uniform distributions in the selection time interval, respectively.

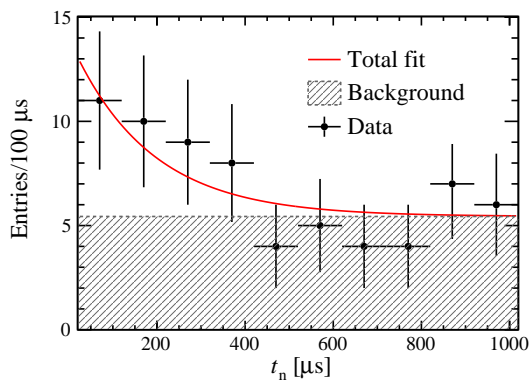
Fig. 8 shows the projected energy and time distributions obtained from the two-dimension fit. N_{obs} is determined to be $\omega \times m = 13.6 \pm 5.7$, where the uncertainty is dominated by the statistics of data. We also changed the time range for background event selection to study the uncertainty from the function f_b and the result indicates it is negligible.

To validate the fit result, a counting method is also used to subtract the background from the neutron candidates. We apply a normalization factor k to estimate the background counts in the time range of the signal by scaling events from the time window of background [29]. In this analysis, due to the low rate of muon events, this factor is simplified to the ratio of the interval lengths. The number of neutron signal events is given by

$$N_{\text{obs}} = N_c - k \times N_b, \quad (11)$$



(a)



(b)

FIG. 8. The energy and time interval spectra from the two-dimension likelihood fit result. The data events are selected within $[20, 1020] \mu\text{s}$ time interval from preceding muons. The gray area represents the background distribution estimated by the events far from the muon signals. The dashed line shows the $n\text{H}$ capture signals described by the calorimeter function [28], while the solid line shows the total fit result.

where N_c represents the number of neutron candidates, N_b represents the number of background events.

For this method, the events within $[1.5, 2.9] \text{ MeV}$, approximating the $\pm 3\sigma$ energy region of 2.2-MeV γ observed in the detector, are used. By counting the event number in different time window, N_c is 23.0 ± 4.8 while N_b is 121.0 ± 11.0 in the data. As the normalization factor k is calculated as 0.1, 10.5 ± 4.9 neutron signals are obtained, where the dominant uncertainty for N_{obs} is from the statistics of N_c , which contributes 99.7% in total. The results from these two methods are consistent, but the fit method gives a better precision.

C. Efficiencies, Correction Factors and Uncertainties

In addition to the number of candidates from event selection and background subtraction, parameters such as the average muon path length, efficiencies, and correction factors also

significantly impact the measurement results of cosmogenic neutron yield. This section focuses on evaluating the nominal values and uncertainties of these parameters. Systematic uncertainties are examined by comparing the variations in values for different detector geometries, muon generators, and physical models used in the simulations. The energy scale uncertainty has already been accounted for in the fitted signal number from the previous section by incorporating it into Eq. 8.

In this study, the average path length L_{avg} of muons is derived from the detector simulations, as described in Sec. III. Following the application of the muon selection criteria detailed in Sec. V, L_{avg} in the LS is calculated to be approximately 95.6 cm. A variation of 0.5 cm in the acrylic vessel radius can alter the target volume of LS, resulting in a 1.4% uncertainty in L_{avg} . The energy scale, which influences the selection of muons based on their energy, can affect the muon candidates, and subsequently, L_{avg} . This impact was assessed using the MC sample, revealing that a 5% uncertainty in the energy scale introduces a 0.6% uncertainty in L_{avg} . Additionally, variations between primary muon can lead to a 0.3% uncertainty due to the slight differences of angular distribution. Finally, the total uncertainty in L_{avg} is determined to be 1.5%.

The neutron trigger efficiency, ε_{nt} , is derived from the MC sample to account for the trigger efficiency of 2.2-MeV γ from $n\text{H}$ captures. Due to the varying operational states of the detector, as outlined in Table I, ε_{nt} exhibits slight variations across different periods. We calculated ε_{nt} for each period, and the weighted average over the effective DAQ time is used for the final measurement. The dominant uncertainty of ε_{nt} is from the variation in the target volume's radius, and evaluated to be 1.4%.

The time selection efficiency, ε_{t} , is also derived from the simulations to account for the impact of time selection. The time interval between the muon and neutron events is determined by the neutron generation time t_g and the neutron capture time t_c . Only t_g varies slightly for the three physical models used in the simulation, with differences on the order of sub-nanoseconds, which are very short compared to t_c . Consequently, the total uncertainty in ε_{t} is evaluated as 0.8% which is from the MC statistics.

1. Non-Target Correction

Neutrons produced by tagged muons in the non-LS region within the detector can be captured in the non-LS region. The main contribution of this effect is from the water and acrylic materials. The gamma rays emitted in this process may enter the LS and generate a trigger that passes the selection criteria. In that case, they will coincide with the tagged muon and be included in the candidate as background events. To account for this effect, we define a non-target correction factor $f_{\text{non-target}}$ as the ratio of the number of gammas emitted by neutrons generated outside the LS and then also captured outside the LS that enter the LS to the total number of gammas candidates.

2. Shower Correction

Muons can produce showers in the water, lead shielding, and rock, generating secondary particles with high kinetic energy, such as fast neutrons. Although these muons do not traverse the LS, some events are still incorrectly tagged as muon signals due to the muon shower, and the subsequent neutron captures are included in the data sample. The factor f_{shower} is used to correct this effect and is evaluated in the MC sample as the ratio of the number of neutron candidates following the muon shower events to those following muon showers or traversing muons. In the simulation, approximately 2.0% of tagged muon events are associated with muon showers, resulting in 21.0% of neutron captures following shower events out of all captures. High-energy neutrons and gammas contribute about 80% and 20%, respectively.

3. Neutron Spill Correction

The neutron spill factor f_{spill} is applied to account for the net effect of spill-in and spill-out of neutrons induced by muons. Neutrons produced inside the LS by tagged muons can propagate to escape the LS before being captured and are treated as spill-out neutrons. In contrast, neutrons produced outside the LS can propagate to be captured inside the LS and be regarded as spill-in neutrons. Additionally, the secondary high-energy particles induced by muons outside the LS can spill into the LS and produce neutrons. This process can also contribute 47.0% to the spill-in neutrons. The correction factor f_{spill} is derived in simulation as the ratio of the number of neutrons produced in the LS due to the muon's passage, to the number of neutrons captured in the LS.

4. Uncertainties of $f_{\text{non-target}}$, f_{shower} , and f_{spill}

The values of correction factor $f_{\text{non-target}}$, f_{shower} , and f_{spill} could differ with various combinations of neutron yields in LS and other materials. The predicted neutron yields in materials vary among the three physical models in the simulation, providing an estimation of the systematic uncertainties for these three factors. Each factor is derived from three MC samples using these three physical models, in which the differences in the values are considered as systematic uncertainties. The uncertainties from MC statistics are subdominant but are still included in the final results. For $f_{\text{non-target}}$, an 8.5% uncertainty comes from physical models, and 3.5% is from MC statistics. For f_{shower} , 9.7% of the uncertainty is addressed by comparing results between different physical models, while 1.4% comes from MC statistics. For f_{spill} , a 6.4% uncertainty is induced by differences in physical models, and 4.7% originates from MC statistics.

To validate the estimations of these factors from MC simulations, we need to compare the cosmogenic neutron yields in LS and other materials obtained from the existing measurements with those used in the simulation. For muons reaching CJPL-I with an average energy of ~ 360 GeV, there is

no measurement of neutron yield in LS before. Therefore, an extrapolation method is applied to the previous measurements at low muon energies. Using the measured results from Hertenberger [30], Bohem [31], Daya Bay (DYB) [29], Aberdeen Tunnel [32], KamLAND [33], LVD [34] with corrections [10], Borexino [35], we fit the relation between average muon energies and neutron yields in LS with a power-law formula [10, 29, 36]. The uncertainties of measurements in each experiment are considered. The cosmogenic neutron yield at CJPL-I is extrapolated based on the fit results, which can be expressed numerically as $(3.57 \pm 0.66) \times 10^{-4} \mu^{-1} \text{g}^{-1} \text{cm}^2$. The secondary particles produced by muons in water are dominant sources accounting for the above three factors. For water, the measurement of SNO in heavy water $(7.28^{+1.68}_{-1.21}) \times 10^{-4} \mu^{-1} \text{g}^{-1} \text{cm}^2$ can be taken as the reference value, which corresponds to the similar average muon energy with CJPL-I and is slightly larger than the yield in water due to the additional neutrons produced in $\gamma(d, n)p$ reactions induced by muons [9]. In the GEANT4 simulation, the neutron yields are calculated to be $(3.65 \pm 0.52) \times 10^{-4} \mu^{-1} \text{g}^{-1} \text{cm}^2$ and $(5.27 \pm 0.75) \times 10^{-4} \mu^{-1} \text{g}^{-1} \text{cm}^2$, respectively for in LS and in water, where the variation of results in the three physical models is taken as uncertainty. By comparison, those used in the simulation are both consistent with the reference values within the uncertainties.

5. Finite-Size Effect

For the production of neutrons in the LS induced by muons reaching CJPL-I, the direct muon spallation with carbon nuclei only contributes about 3.8% in simulation, while the dominant parts come from the indirect processes initiated by muon-induced secondary particles, such as high-energy gammas. Due to the finite size of the detector, secondary particles produced by muons in the LS can escape from the target volume, LS. If the detector size were slightly enlarged, these secondary particles might generate additional neutrons, which should be included when evaluating the neutron yield. While this additional neutron production contributes negligibly to the neutron yield in large detectors, it can be visible in small-size detectors, like in the 1-ton prototype. To ensure a consistent definition of neutron yield with other experiments and to make the measured yield independent of detector size, this effect is studied in detail and then corrected for the neutron yield measurement.

We construct a spherical detector with an 8-meter radius filled with LS in GEANT4 to study this effect. The volume within a sphere of the 0.645-meter radius is considered as the target region of the 1-ton prototype, while the volume outside is treated as the buffer region. The tracks of secondary particles produced inside the target region due to the passage of muons are recorded. When counting neutrons, the $(n, 2n)$ reaction increases the neutron number by 1, while the (n, n') reaction does not change the neutron number. To correct for the finite-size effect described above, we calculate the factor

f_{size} as follows:

$$f_{\text{size}} = \frac{N_{\text{in}}}{N_{\text{in}} + N_{\text{out}}}, \quad (12)$$

where N_{in} is the number of neutrons produced by muons inside the target region, either directly or indirectly, and N_{out} is the number of neutrons generated in the buffer region by secondary particles of muons emitted from the target region.

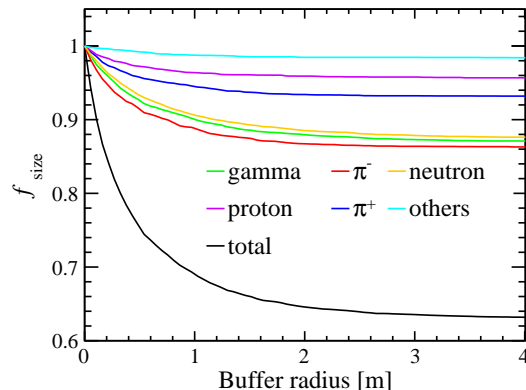


FIG. 9. The finite-size correction factor f_{size} varies with the radius of buffer region in the simulation. The contributions of different particles to this factor are also plotted.

The factors f_{size} for different buffer region radii are estimated using the MC sample and shown in Fig. 9. The results indicate that a buffer region with at least a 3-meter radius is required for the detector, which is also taken as the nominal value of the factor f_{size} in the measurement. The contributions of different secondary particles are also depicted in Fig. 9. The inelastic scatterings of muon-induced secondary high-energy particles on carbon nuclei are the dominant sources of this effect, including protons, neutrons, and positive and negative pions (π^+ and π^-). For π^- , thermal captures on carbon and hydrogen nuclei, such as the $\pi^-(p, n)\pi^0$ reaction, also contribute to this effect. Photonuclear disintegration on carbon nuclei, typically the $\gamma(^{12}\text{C}, ^{11}\text{C})n$ reaction, is another significant source. Other high-energy particles like electrons, positrons, deuterons, tritons, and strange hadrons also make few contributions through inelastic scatterings. Additionally, muons can generate radioactive nuclei in the LS, such as ^4H , which can produce neutrons through decay. However, these nuclei are unlikely to spill out before decaying due to their heavy mass, thus contributing minimally to the correction factor. The particle composition accounting for this effect is similar to that in previous simulation studies for cosmogenic neutrons [36].

The yields of secondary particles produced by muons and the neutron yield of secondary particles in LS could differ among the three physical models. Therefore, the factor f_{size} is studied using each of the three models, with numerical differences amounting to 1.4% covered by the statistical uncertainty of 1.3%. This factor is sensitive to the detector size. A 5 mm

variation in the detector radius, which corresponds to the parameter uncertainty of the acrylic vessel radius, can induce a 0.3% uncertainty in f_{size} . The total uncertainty of f_{size} is thus estimated to be 1.3%, calculated as the quadratic sum of the two components.

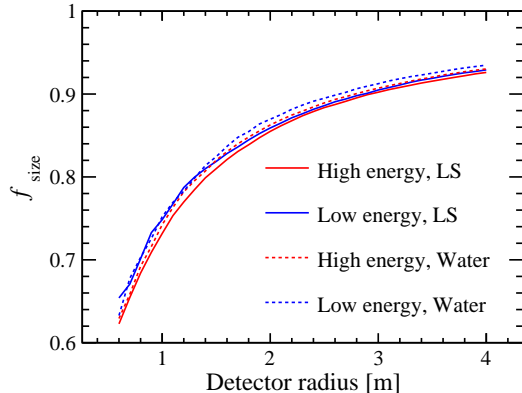


FIG. 10. The finite-size correction factor f_{size} varies with the detector size, while the radius of the buffer region outside the detector is fixed at 3 m. The red lines represent the muons with ~ 360 GeV average energy corresponding to the muons arriving CJPL-I. The blue lines show the low-energy muons with 70 GeV average energy. The correction factor in LS- and water-based detectors are plotted with solid and dashed lines, respectively.

Furthermore, the radius of the target region was also varied with a fixed buffer region of 3 meters to study the relationship between the correction factor and detector size. The result, shown in Fig. 10, demonstrates that this effect is sensitive to detector size. Additionally, we also studied the impact of different average muon energies and target materials. For experiments with shallow overburden such as the experimental hall-1(EH1) of Daya Bay, where the average muon energy is about 70 GeV [29], this effect is slightly weakened, primarily due to the increased ratio of neutrons produced through direct inelastic scattering by low-energy muons [36]. This effect is also weaker in water than in LS due to secondary particles' shorter average free path. For example, in simulations, the average free path of secondary gamma rays produced by muons in water is calculated to be 46.6 cm, while this parameter is 66.5 cm in LS, resulting in fewer spill-out of gammas.

This effect could also be significant for measuring other cosmogenic production yields in small-size detectors, such as for ${}^9\text{Li}$ and ${}^8\text{He}$. These radioactive isotopes are predominantly produced by secondary particles like π^- induced by muons [8].

Table III summarizes the correction factors, efficiencies, and other parameters with their uncertainties.

Parameter	Nominal value	Uncertainty	Dominant source
ε_{nt}	63.8%	$\pm 1.4\%$	Acrylic vessel radius
ε_{t}	90.6%	$\pm 0.8\%$	MC statistic
$f_{\text{non-target}}$	0.24	$\pm 9.2\%$	Hadronic model
f_{shower}	0.21	$\pm 9.8\%$	Hadronic model
f_{spill}	0.61	$\pm 7.9\%$	Hadronic model
f_{size}	0.63	$\pm 1.9\%$	MC statistic
L_{avg}	95.6 cm	$\pm 1.3\%$	Acrylic vessel radius
ρ	0.86 g/cm ³		
Total		$\pm 9.3\%$	

TABLE III. The nominal value and systematic uncertainty of parameters used in the measurement of cosmogenic neutron yield, in which the dominant source of uncertainty is also stated.

D. Result

The cosmogenic neutron yield in liquid scintillator at CJPL-I is measured to be

$$Y_{\text{n}} = (3.37 \pm 1.41_{\text{stat.}} \pm 0.31_{\text{sys.}}) \times 10^{-4} \mu^{-1} \text{g}^{-1} \text{cm}^2. \quad (13)$$

The corresponding average muon energy is derived from simulation as 360 ± 10 GeV, which indicates that this work provides the world's highest average muon energy measurement of cosmogenic neutron yield in LS. The uncertainty of average muon energy mainly comes from the differences between two muon generators, MCEq and the modified Gaisser' formula, while the laboratory elevation uncertainty also has contributions. The uncertainty of this yield measurement is dominant by data statistic, contributing 95% in total, while the systematic uncertainty has 5% contributions.

The cosmogenic neutron yields of different LS detectors in terms of average muon energy are shown in Fig. 11. The relation between average muon energy and neutron yield can be described by the empirical formula from previous studies [10, 29, 36], written as

$$Y_{\text{n}} = a \times E_{\mu}^b, \quad (14)$$

where a and b are fitting parameters. A global fit with the measurement of this work and previous experiments in LS [29–35], is processed in which the uncertainties of E_{μ} and Y_{n} are both considered. For the results in other experiments without E_{μ} uncertainty, zero uncertainty is assumed at this point in the fit. The fit result shows that

$$a = (3.9 \pm 0.7) \times 10^{-6} \mu^{-1} \text{g}^{-1} \text{cm}^2, b = 0.77 \pm 0.03, \quad (15)$$

which is consistent with previous study within the range of uncertainty [29].

VII. SUMMARY AND DISCUSSION

In this work, we studied the cosmic muons reaching CJPL-I using 1178 days of data collected by the 1-ton prototype neutrino detector for the Jinping Neutrino Experiment. Comprehensive simulations were also conducted to understand the

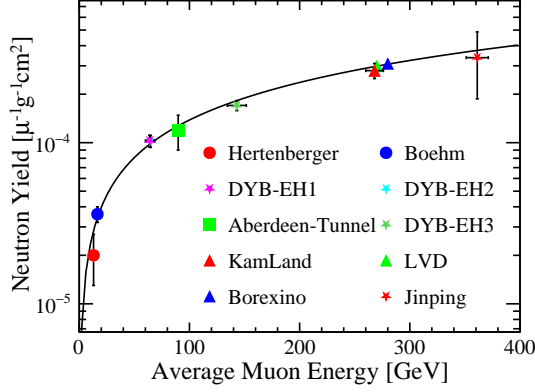


FIG. 11. The cosmogenic neutron yield as a function of average muon energy from this study is compared with results from other experiments. The solid line represents the global fit obtained using the power-law formula.

interaction processes of muons with mountain rocks and the detector. Through a thorough evaluation of detection efficiency and uncertainties, particularly the detector's finite-size effect, this study determined the cosmic muon flux to be $(3.56 \pm 0.16_{\text{stat.}} \pm 0.10_{\text{sys.}}) \times 10^{-10} \text{ cm}^{-2}\text{s}^{-1}$ at CJPL-I and the cosmogenic neutron yield in liquid scintillator to

be $(3.37 \pm 1.41_{\text{stat.}} \pm 0.31_{\text{sys.}}) \times 10^{-4} \mu^{-1}\text{g}^{-1}\text{cm}^2$ with $\sim 360 \text{ GeV}$ average muon energy. The reconstructed angular distribution of muons suggests that muon leakage is consistent with the expected influence of the mountain topography near CJPL-I.

This study innovatively addresses the challenges of measuring the cosmogenic production yield in a small-size LS detector, which should be valuable for the related study in other experiments. A measurement of cosmogenic neutron yield for LS is presented with the highest average muon energy in the world. The measurement results will serve as important references for conducting low-background experiments in the future at CJPL.

VIII. ACKNOWLEDGEMENTS

This work was supported in part by the National Natural Science Foundation of China (12127808, 12141503 and 12305117) and the Key Laboratory of Particle and Radiation Imaging (Tsinghua University). We acknowledge Orrin Science Technology, Jingyifan Co., Ltd, and Donchamp Acrylic Co., Ltd, for their efforts in the engineering design and fabrication of the stainless steel and acrylic vessels. Many thanks to the CJPL administration and the Yalong River Hydropower Development Co., Ltd. for logistics and support.

-
- [1] J.-P. Cheng *et al.*, *Ann. Rev. Nucl. Part. Sci.* **67**, 231 (2017), arXiv:1801.00587 [hep-ex].
 - [2] J. F. Beacom *et al.* (JNE), *Chin. Phys. C* **41**, 023002 (2017), arXiv:1602.01733 [physics.ins-det].
 - [3] C. Galbiati, A. Pocar, D. Franco, A. Ianni, L. Cadonati, and S. Schonert, *Phys. Rev. C* **71**, 055805 (2005), arXiv:hep-ph/0411002.
 - [4] M. Agostini *et al.* (Borexino), *Eur. Phys. J. C* **81**, 1075 (2021), arXiv:2106.10973 [physics.ins-det].
 - [5] M. Agostini *et al.* (Borexino), *Eur. Phys. J. C* **80**, 1091 (2020), arXiv:2005.12829 [hep-ex].
 - [6] K. Abe *et al.* (Super-Kamiokande), *Phys. Rev. D* **94**, 052010 (2016), arXiv:1606.07538 [hep-ex].
 - [7] M. Agostini *et al.* (Borexino), *Phys. Rev. D* **101**, 062001 (2020), arXiv:1709.00756 [hep-ex].
 - [8] Y. Zhang *et al.* (Super-Kamiokande), *Phys. Rev. D* **93**, 012004 (2016), arXiv:1509.08168 [hep-ex].
 - [9] B. Aharmim *et al.* (SNO), *Phys. Rev. D* **100**, 112005 (2019), arXiv:1909.11728 [hep-ex].
 - [10] D. Mei and A. Hime, *Phys. Rev. D* **73**, 053004 (2006), arXiv:astro-ph/0512125.
 - [11] Y. Wu *et al.*, *Nucl. Instrum. Meth. A* **1054**, 168400 (2023), arXiv:2212.13158 [hep-ex].
 - [12] Z. Wang *et al.*, *Nucl. Instrum. Meth. A* **855**, 81 (2017), arXiv:1703.01478 [physics.ins-det].
 - [13] Z. Guo *et al.*, *Astropart. Phys.* **109**, 33 (2019), arXiv:1708.07781 [physics.ins-det].
 - [14] W. Luo *et al.*, *JINST* **18** (02), P02004, arXiv:2209.13772 [physics.ins-det].
 - [15] S. Agostinelli *et al.* (GEANT4), *Nucl. Instrum. Meth. A* **506**, 250 (2003).
 - [16] J. Allison *et al.*, *IEEE Trans. Nucl. Sci.* **53**, 270 (2006).
 - [17] M. Guan, M.-C. Chu, J. Cao, K.-B. Luk, and C. Yang, *A parametrization of the cosmic-ray muon flux at sea-level* (2015), arXiv:1509.06176 [hep-ex].
 - [18] A. Fedynitch, R. Engel, T. K. Gaisser, F. Riehn, and T. Stanev, *EPJ Web Conf.* **99**, 08001 (2015), arXiv:1503.00544 [hep-ph].
 - [19] A. Fedynitch, F. Riehn, R. Engel, T. K. Gaisser, and T. Stanev, *Phys. Rev. D* **100**, 103018 (2019), arXiv:1806.04140 [hep-ph].
 - [20] T. G. Farr *et al.*, *Reviews of Geophysics* **47** (2007).
 - [21] M. Zheng, S. Li, Z. Feng, H. Xu, and Y. Xiao, *International Journal of Mining Science and Technology* **34**, 179 (2024).
 - [22] W. M. Haynes, *CRC Handbook of Chemistry and Physics*, Vol. 97 (CRC Press, 2016).
 - [23] S. W. Li and J. F. Beacom, *Phys. Rev. D* **91**, 105005 (2015), arXiv:1503.04823 [hep-ph].
 - [24] E. H. Bellamy *et al.*, *Nucl. Instrum. Meth. A* **339**, 468 (1994).
 - [25] L. Zhao *et al.* (JNE), *Chin. Phys. C* **46**, 085001 (2022), arXiv:2108.04010 [hep-ex].
 - [26] Z. Guo *et al.* (JNE), *Chin. Phys. C* **45**, 025001 (2021), arXiv:2007.15925 [physics.ins-det].
 - [27] B. Zhang, Z. Wang, and S. Chen, *Applied Sciences* **12**, 10.3390/app122110975 (2022), arXiv:2209.11974.
 - [28] J.-H. Cheng *et al.*, *Nucl. Instrum. Meth. A* **827**, 165 (2016), arXiv:1603.04433 [physics.ins-det].
 - [29] F. P. An *et al.* (Daya Bay), *Phys. Rev. D* **97**, 052009 (2018), arXiv:1711.00588 [hep-ex].
 - [30] R. Hertenberger, M. Chen, and B. L. Dougherty, *Phys. Rev. C* **52**, 3449 (1995).

- [31] F. Boehm *et al.*, *Phys. Rev. D* **62**, 092005 (2000), [arXiv:hep-ex/0006014](#).
- [32] S. C. Blyth *et al.* (Aberdeen Tunnel Experiment), *Phys. Rev. D* **93**, 072005 (2016), [Addendum: *Phys.Rev.D* 94, 099906 (2016)], [arXiv:1509.09038 \[physics.ins-det\]](#).
- [33] S. Abe *et al.* (KamLAND), *Phys. Rev. C* **81**, 025807 (2010), [arXiv:0907.0066 \[hep-ex\]](#).
- [34] M. Aglietta *et al.* (LVD), in *26th International Cosmic Ray Conference* (1999) [arXiv:hep-ex/9905047](#).
- [35] G. Bellini *et al.* (Borexino), *JCAP* **08**, 049, [arXiv:1304.7381 \[physics.ins-det\]](#).
- [36] Y. F. Wang, V. Balic, G. Gratta, A. Fasso, S. Roesler, and A. Ferrari, *Phys. Rev. D* **64**, 013012 (2001), [arXiv:hep-ex/0101049](#).